Available online at www.sciencedirect.com
ScienceDirect
Trans. Nonferrous Met. Soc. China 35(2025) 2341−2353
Transactions of Nonferrous Metals Society of China
www.tnmsc.cn

High-performance $Li_3YCl_3Br_3$ halide solid electrolyte synthesized using wet-chemistry route for all-solid-state battery

Han-zhou LIU[1], Yan-chen LIU[1], Sheng-hao JING[1], Ya-qi HU[1], Zong-liang ZHANG[2], Si-liang LIU[3], Yang LIU[4], Zhi ZHUANG[4], Fan-qun LI[5], Fang-yang LIU[1,6]

1. School of Metallurgy and Environment, Central South University, Changsha 410083, China;
2. Hunan Provincial Key Laboratory of Nonferrous Value-added Metallurgy, Central South University, Changsha 410083, China;
3. Advanced Battery Materials Engineering Research Center of the Ministry of Education, Central South University, Changsha 410083, China;
4. Hunan Energy Frontiers New Materials Technology Co., Ltd., Changsha 410208, China;
5. Wanxiang 123 Co., Ltd., Hangzhou 311200, China;
6. National Key Laboratory of Energy, Metal Resources and New Materials, Central South University, Changsha 410083, China

Received 7 May 2024; accepted 11 December 2024

Abstract: A dual-halide solid electrolyte, $Li_3YCl_3Br_3$, was synthesized using a wet-chemistry route instead of the conventional mechanical ball-milling route. $Li_3YCl_3B_{r3}$ exhibits an ion conductivity of 2.08 mS/cm and an electrochemical stability window of 3.8 V. Additionally, an all-solid-state lithium-ion battery using $Li_3YCl_3Br_3$ and $LiNi_{0.83}Co_{0.11}Mn_{0.06}O_2$ (NCM811) as the cathode material achieves a capacity retention of 93% after 200 cycles at 0.3*C* and maintains a specific capacity of 115 mA·h/g during 2*C* cycling. This exceptional performance is attributed to the high oxidative stability of $Li_3YCl_3Br_3$ and the in-situ formation of Y_2O_3 inert protective layer on the NCM811 surface under high voltage. Consequently, the study demonstrates the feasibility of a simple, cost-effective wet-chemistry route for synthesizing multi-component halides, highlighting its potential for large-scale production of halide solid electrolytes for practical applications.

Key words: halide solid electrolytes; all-solid-state batteries; wet-chemistry route; by-product; inert layer

1 Introduction

Currently, commercial lithium-ion batteries have found widespread applications in industries such as electronic devices and electric vehicles; however, they are confronted with developmental challenges of insufficient energy density and inadequate safety measures [1−3]. Therefore, all-solid-state lithium-ion batteries (ASSLBs) have emerged as the most promising solution and have become a significant area of research in recent years [4,5].

As the crucial component of the ASSLBs, the solid electrolyte has been extensively investigated, including oxides, polymers, sulfides, and emerging halides. Oxide solid electrolytes exhibit high electrochemical stability but suffer from poor processability and relatively low ionic conductivity [6−8]. Polymer solid electrolytes offer excellent processability but are hampered by low room-temperature ionic conductivity and insufficient

Corresponding author: Fang-yang LIU, Tel: +86-13974914406, E-mail: liufangyang@csu.edu.cn
https://doi.org/10.1016/S1003-6326(25)66819-1

electrochemical stability [9,10]. Although the sulfide solid electrolytes exhibit both excellent process-ability and high ionic conductivity, their electrochemical window is relatively narrow, typically ranging from 1.7 to 2.2 V [11−15]. In contrast, halide solid electrolytes possess an electrochemical window that can exceed 4 V, along with commendable ionic conductivity and process-ability. Consequently, halide solid electrolytes show great potential for application in ASSLBs [16−18].

The rapid development of the halide solid electrolytes in recent years can be attributed to the research conducted by Panasonic Corporation in 2018, focusing on Li_3YCl_6 and Li_3YBr_6 [16]. Subsequently, LI et al [19,20] reported the synthesis of Li_3InCl_6 (LIC) electrolytes using aqueous solution. Expanding upon the halide Li−M−X systems (M=metal element, and X=F, Cl, Br, and I), many groups have explored various intermediate metal elements M. For example, Li_xScCl_{3+x} with a ccp structure was successfully prepared, demonstrating a high ionic conductivity of 3 mS/cm [21]. LIU et al [22] has reported the successful preparation of $Li_3YCl_3Br_3$ electrolyte through hot pressing and sintering techniques, resulting in an impressive ion conductivity of 7.2 mS/cm. Furthermore, several halide solid electrolytes, including $Li_{3-x}Yb_{1-x}Zr_xCl_6$ [23], Li_2ZrCl_6 [24], $Li_{2.25}Zr_{0.75}Fe_{0.25}Cl_6$ [25], $Li_{2.9}In_{0.9}Zr_{0.1}Cl_6$ [26], $Li_{3-x}Er_{1-x}Zr_xCl_6$ [27], and $Li_2In_{0.444}Sc_{0.222}Cl_4$ [28], have also emerged.

The performance of halide solid electrolytes currently demonstrate significant potential for industrial applications [29]. However, the widespread reliance on the mechanical ball-milling method for the preparation of halide solid electrolytes has emerged as a significant bottleneck. This challenge, similar to that encountered with sulfide electrolytes, continues to hinder their broader adoption. In contrast, the wet chemistry synthesis approach offers a more efficient and productive technique for solid electrolyte preparation compared to mechanical ball-milling. Existing reports indicate that among halide electrolytes, only LIC can be directly synthesized through a pure aqueous system [19]. Additionally, ammonia-assisted solution precursor method has been employed for synthesizing specific halide electrolytes [30]. In 1989, MEYER et al [31] reported generation of $(NH_4)_3[MCl_6]$ (M=Tb−Lu, Y, Sc) in an aqueous solution using $YCl_3·6H_2O$ and NH_4Cl. Subsequently, WANG et al [30] utilized this method to synthesize electrolytes such as LYC, Li_3ErCl_6, and Li_3ScCl_6, through the reaction of $(NH_4)_3[MCl_6]$ with LiX (X=Cl, Br).

The wet chemistry synthesis route exhibits significant potential for industrial applications, deserving more attention as the performance of halide solid electrolytes continues to improve. In this study, the precursor $(NH_4)_3[YCl_3Br_3]$ was successfully synthesized using ammonia solution, and the $Li_3YCl_3Br_3$ (LYCB) electrolyte was prepared through high-temperature sintering of the precursor. Furthermore, the electrochemical performance of LYCB and the performance of LYCB-based ASSLBs were investigated. To our knowledge, LYCB in this work represents the first reported instance of a dual-halide solid-state electrolyte synthesized via a wet chemical route. We hope that this work can offer new perspectives and provide practical examples for the wet-chemical preparation of halide electrolytes.

2 Experimental

2.1 Materials preparation

Inspired by work of WANG et al [30], LYCB was synthesized from $YCl_3·6H_2O$ (Aladdin, 99.99%), NH_4Br (Aladdin, 99.99%), and LiBr (Aladdin, 99.9%). Firstly, $YCl_3·6H_2O$, NH_4Br, and LiBr were weighed according to the molar ratio of 1∶3∶3, and then dissolved in deionized water and heated and stirred for 10 min to obtain the precursor solution. Then, the precursor solution was dried under a vacuum at 120 °C for 24 h to obtain the precursor powder. Subsequently, the precursor was sintered in a furnace at 450 °C for 6 h to obtain the LYCB electrolyte (in an argon atmosphere glove box). Li_3YCl_6 (LYC) was synthesized from $YCl_3·6H_2O$ (Aladdin, 99.99%), NH_4Cl (Aladdin, 99.99%), and LiCl (Aladdin, 99.99%), and the synthesis steps were the same as those of LYCB, except that the sintering temperature was increased to 500 °C. Li_3YBr_6 (LYB) was synthesized from YBr_3 (Aladdin, 99.99%), NH_4Br (Aladdin, 99.99%), and LiBr (Aladdin, 99.99%), and the synthesis steps were identical to those of LYCB.

The ball-milled $Li_3YCl_3Br_3$ (BM-LYCB) was synthesized from YCl_3 (Aladdin, 99.99%) and LiBr (Aladdin, 99.9%). Firstly, the YCl_3 and LiBr were

weighed in a molar ratio of 1∶3 and placed into a zirconia ball mill of 250 mL. The material-to-ball ratio is 1∶30, utilizing zirconia balls with a diameter of 5 mm. The mixture was then ball-milled at a rotation speed of 400 r/min for 10 h. Subsequently, it was subjected to annealing at 400 °C in a furnace for 8 h to obtain BM-LYCB electrolyte (inside an argon gas atmosphere glove box). The preparation process for Li_3YBr_6 (BM-LYB) is the same as BM-LYCB, except that YBr_3 is used instead of YCl_3. Li_3YCl_6 (BM-LYC) was synthesized employing the same ball milling process as used for BM-LYCB, without subsequent heat treatment, with YCl_3 and LiCl used as the precursor materials.

The Li_6PS_5Cl (LPSC) was synthesized from Li_2S (Hunan Energy Frontiers New Materials Technology Co., Ltd. (China), 99.9%), P_2S_5 (Hunan Energy Frontiers New Materials Technology Co., Ltd. (China), 99.9%), and LiCl (99.9%, Aladdin). Li_2S, P_2S_5, and LiCl are mixed in a molar ratio of 5∶1∶2 and placed in a zirconia ball mill jar of 250 mL. The material-to-ball ratio is 1∶30, utilizing zirconia balls with a diameter of 5 mm. The mixture is ball-milled at a rotational speed of 400 r/min for 4 h. Subsequently, it is transferred to the furnace and sintered at 500 °C for 8 h to obtain electrolyte (inside an argon gas atmosphere glove box).

2.2 Assembly of batteries

For the cyclic voltammetry (CV) cell, a certain amount of LYX (LYCB, LYC and LYB) electrolyte and VGCF is weighed in a mass ratio of 9∶1. They are thoroughly mixed and manually ground for 10 min to obtain a composite cathode. The composite cathode powder, LYX electrolyte powder, and indium foil are sequentially layered in a 10 mm diameter mold and then compacted into a solid block using a pressure of 620 MPa. The block is assembled into a button cell along with lithium foil and SUS current collector. The mass of the composite cathode powder is approximately 10 mg, the mass of LYX powder is around 200 mg, the thickness of the indium foil is about 100 μm, and the mass of the lithium foil is approximately 1.5 mg.

For the ASSLBs, a certain amount of NCM811, LYX electrolyte, and vapor-grown carbon fiber (VGCF, Showa Denko) is weighed in a mass ratio of 60∶37∶3. They are thoroughly mixed and manually ground for 10 min to obtain a composite cathode. For battery assembly, in a 10 mm diameter mold, the composite cathode powder, LYX electrolyte powder, LPSC electrolyte powder, and indium foil are sequentially layered and then compacted into a solid block using a pressure of 620 MPa. The block is assembled into a button cell along with lithium foil and SUS current collector. The mass of the composite cathode powder is approximately 10 mg, the mass of LYX powder is around 70 mg, the mass of LPSC powder is around 90 mg, the thickness of the indium foil is about 100 μm, and the mass of the lithium foil is approximately 1.5 mg.

2.3 Structure and morphology characterizations

The crystal structure of the electrolyte was characterized using X-ray diffraction (XRD; Rigaku, MiniFlex600) with Cu K_α radiation with a wavelength of 0.154 nm. Rietveld refinement was performed using GSAS II. X-ray photoelectron spectroscopy (XPS; ULVAC-PHI, PHI VersaProbe 4) with Al K_α microfocused monochromatic source was employed to determine the state of the analyzed substances. Calibration was performed using the surface contaminant C 1s (284.8 eV) as a reference standard. The morphology and composition of the samples were examined using field emission scanning electron microscopy (FE-SEM; JOEL, JSM7610FPlus) with the accelerating voltage of 5 kV and energy-dispersive X-ray spectroscopy (EDS; Oxford, Ultim Max40). All of the aforementioned equipment was operated within a vacuum transfer box to avoid exposure to air. The composite cathode of the ASSLBs before and after cycling was observed using focused ion beam scanning electron microscopy (FIB-SEM; ZEISS Crossbeam 540). The phase evolution of NCM811 grains before and after cycling was observed using transmission electron microscopy (TEM; Talos F200X) with a accelerating voltage of 200 kV.

2.4 Electrochemical measurements

The ionic conductivity of materials and the electrochemical impedance spectroscopy (EIS) data of the ASSLBs were collected using Gamry Reference 600+ with 30 mV amplitude. Before conducting conductivity measurements, approximately 200 mg of solid electrolyte powder is placed into a polyether-ether-ketone (PEEK)

mold with a diameter of 10 mm inside an Ar-filled glove box. The mold is then pressed using a hydraulic press at 430 MPa for 3 min. During the EIS testing of ASSLBs, a pressure of 20 MPa was applied. The direct current (DC) polarization data of the electrolytes were collected using Gamry Reference 600+ at a voltage of 1 V. The CV measurement of cells was tested using a potentiostat (Admiral, Squidstat Prime) at a scan rate of 0.1 mV/s in the potential range of 2−3.9 V or 2.0−4.0 V versus Li−In at 25 °C, During the CV testing, an external pressure of 20 MPa is applied to the cell. The electrochemical performance of LYX ASSLBs was measured with a multichannel battery test system (LAND, CT−2001A) at 25 °C. Galvanostatic measurements were performed with 0.1*C* rate for the first turns and then cycling at 0.3*C* rate (1*C*=170 mA/g). During the cycling, an external pressure of 20 MPa is applied to the cell.

3 Results and discussion

3.1 Synthesis and phase structure of LYCB

The precursors of LYCB (P-LYCB) and LYCB electrolyte were synthesized using an ammonia-assisted wet chemistry method. XRD analysis was conducted on P-LYCB, LYCB and the raw materials, as presented in Fig. 1(a). The diffraction peaks of P-LYCB closely match the standard peaks of LiBr and NH_4Br (space group $Pm\bar{3}m$), and no diffraction peaks of $YCl_3·H_2O$ are observed. Based on previous reports, the NH_4Br-like phase is inferred to be $(NH_4)_3YX_6$ (X=Cl, Br) [30]. Furthermore, EDS analysis of P-LYCB (Fig. S1 in Supporting Information (SI)) reveals a uniform distribution of Y, Cl and Br elements in grains, suggesting that NH_4Br-like phase is likely a single-phase compound rather than a mixture of $(NH_4)_3YCl_6$ and $(NH_4)_3YBr_6$. For $(NH_4)_3YCl_6$, it is cataloged as PDF# 04-010-7425 (space group of *C*2/*c*) [30]. Another space group for $(NH_4)_3YCl_6$ is $Pm\bar{3}m$, as indicated by PDF# 04-010-7426. Although no relevant card for $(NH_4)_3YBr_6$ has been found, based on the crystal structure characteristics, it can be anticipated that $(NH_4)_3YCl_3Br_3$ and $(NH_4)_3YBr_6$ likely share the same $Pm\bar{3}m$ space group, similar to NH_4Br. Therefore, it can be concluded that $(NH_4)_3YCl_3Br_3$ is the dominant phase. As shown in Fig. 1(a), the sintered LYCB electrolyte belongs to the same space group as

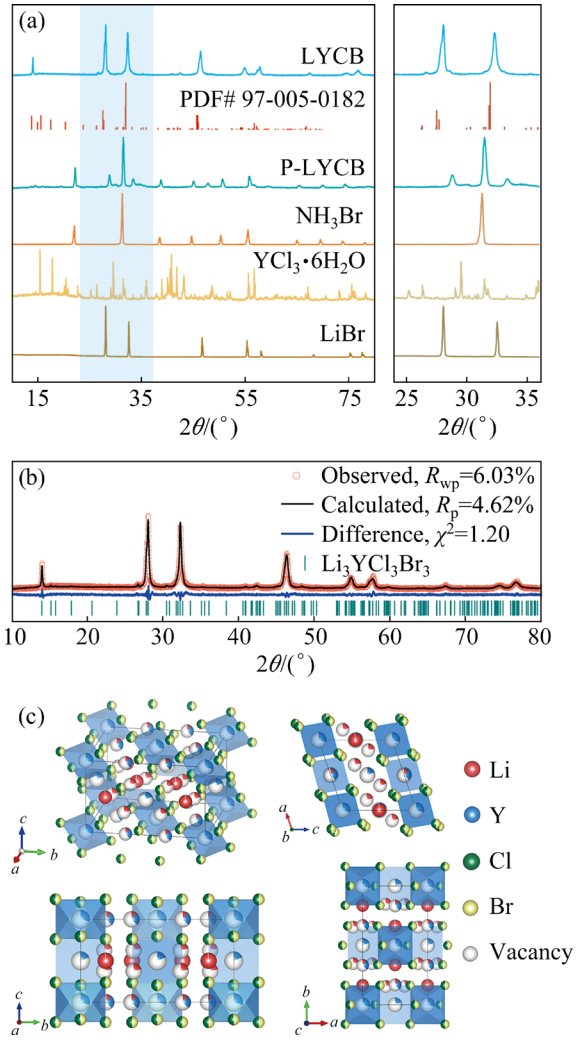

Fig. 1 XRD patterns of raw materials, P-LYCB and LYCB (a); Rietveld refinement of XRD pattern for LYCB (b); Crystal structure of LYCB based on XRD Rietveld refinement result by VESTA (c)

Li_3ErBr_6 (PDF# 97-005-0182, monoclinic, space group *C*2/*m*).

Figure 1(b) displays the refined XRD spectrum of LYCB, revealing no apparent impurity phases (detailed information regarding cell parameters and atomic occupancy can be found in Table S1 in SI). Consequently, it can be inferred that the synthesis of LYCB using the ammonia-assisted wet chemistry method results in minimal precursor segregation, ensuring compositional uniformity from the precursor to the final LYCB electrolyte. Moreover, based on the fine crystal structure data of LYCB, an atomic structure model is constructed, as shown in Fig. 1(c). Notably, lithium ions occupy three sites: 4h, 4g (shared with Y atoms) and 8j. The coexistence of multiple sites for lithium ions leads

to the formation of numerous vacancies, thereby reducing the migration energy barrier for lithium ions [32]. Concurrently, the coexistence of octahedral Li (4h, 4g) and tetrahedral Li (8j) can lead to the formation of tetrahedral or octahedral vacancies. This not only contributes to the energy landscape changes by making it more flat but also potentially triggering a concerted Li^+ diffusion [22,33,34]. However, the occurrence of Li/Y substitution introduces disorder in the crystal structure, leading to a reduction in the structural order of the material. For LYC materials, this phenomenon often enhances their ionic conductivity, but for LYCB, it has the opposite effect [16]. As illustrated in Fig. 1(c), similar to LYB, lithium-ion migration pathways exist in LYCB both in the ab-plane and along the *c*-axis. Therefore, the low degree of order in the material may lead to the disruption of these stable channels, thereby reducing ionic conductivity. While Li/Y substitution may lead to a reduction in structural order, it simultaneously results in the generation of lithium ion vacancies. Consequently, determining the positive impact of this phenomenon on the ionic conductivity of LYB-based materials necessitates further comprehensive investigation. Overall, in comparison to LYB, LYCB exhibits a higher number of vacancies, consequently leading to a further reduction in the migration energy barrier. Therefore, it is anticipated that LYCB can demonstrate superior ionic conductivity when compared to LYB.

3.2 Microstructure and conductivity of LYCB

Figure 2(a) illustrates the grains of LYCB prepared by wet chemistry synthesis and mechanical ball-milling (BM). It can be observed that the crystal sizes of both are at the nano-scale, and the secondary particle size is below 5 μm. The particles of BM-LYCB display a more rounded morphology, whereas the LYCB grains exhibit irregularities, accompanied by a minor presence of flake-like and layered structures. Due to the influence of the milling balls, the grains of BM-LYCB tend to assume a spherical shape, accompanied by a refinement process. However, LYCB undergoes melting and crystallization during the high-temperature reaction of the precursor,

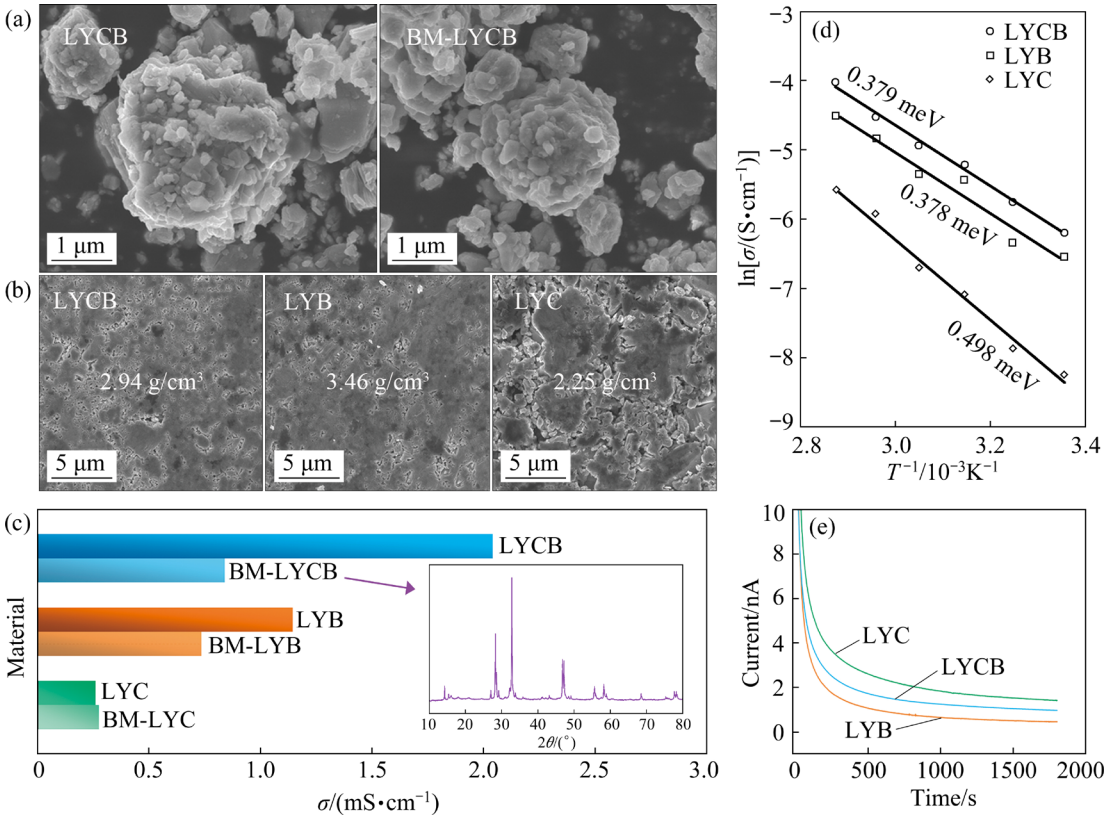

Fig. 2 SEM image of LYCB and BM-LYCB (a); SEM images of surface of LYCB, LYB, and LYC pellets (b); Ionic conductivity of LYCB, LYB, and LYC prepared by wet chemistry method and mechanical ball-milling, and XRD pattern of BM-LYCB (c); Arrhenius plots (d) and DC polarization curves (e) of LYCB, LYB, and LYC

resulting in irregular and flake-like structures. Materials with irregularly shaped grains generally exhibit better processing performance, which helps to increase the compaction density of LYCB. Furthermore, in comparison to LYC and LYB (Fig. S2 in SI), LYCB also exhibits relatively smaller grain sizes. In addition, LYC and LYB prepared by the wet method, as shown in Fig. S2 in SI, also exhibit a plate-like structure, in sharp contrast to the irregular structures of BM-LYC and BM-LYB. Figure 2(b) illustrates the surface morphology of bulk samples of LYCB, LYC and LYB subjected to a pressure of 620 MPa. Evidently, in contrast to LYCB and LYB, the pressed LYC sample retains many voids and pores, which means lower processability. The actual densities of these samples are also provided in Fig. 2(b), revealing a substantial density disparity between LYB and LYC, which belong to different space groups, while LYCB falls in between.

Figure 2(c) presents a column chart comparing the ionic conductivities of LYCB, LYC and LYB prepared via BM and wet chemistry synthesis. It is noteworthy that the annealing temperature for BM-LYX is consistently set at 400 °C. This choice is based on the observation that BM-LYCB achieves its highest ionic conductivity at this temperature, as illustrated in Fig. S3 in SI. Notably, regardless of the preparation method, LYCB consistently exhibits the highest ionic conductivity among the three, especially when prepared using the wet chemistry synthesis, where the ionic conductivity reaches as high as 2.08 mS/cm. It is noteworthy that both LYCB and LYB, synthesized through wet chemistry synthesis, demonstrate higher ionic conductivity compared to those prepared via mechanical ball-milling, with LYCB exhibiting an almost twofold increase.

However, from the XRD diffraction pattern of BM-LYCB, it appears that its crystallinity is slightly higher compared to LYCB. Beyond crystallinity, the impact of grain size and grain boundaries on the ionic conductivity of solid-state electrolyte materials is substantial. LYCB, prepared through hot-press sintering, demonstrates an impressive ionic conductivity reaching up to 7.2 mS/cm [22]. In contrast, the ball-milled LYCB displays a higher quantity of smaller grains, resulting in an increased prevalence of grain boundaries. Additionally, as the annealing process lacks the incorporation of hot-press, the effective enhancement of contact among grain boundaries is not achieved, resulting in higher grain boundary impedance compared to LYCB. This may be a primary factor contributing to the higher ionic conductivity of LYCB compared to BM-LYCB. Figure 2(d) illustrates the activation energies of 0.379, 0.378, and 0.498 eV, respectively, for LYCB, LYB, and LYC. The activation energy of LYCB and LYB is significantly lower than that of LYC. The Nyquist plots of the three electrolytes at room temperature are depicted in Fig. S4 in SI. Figure 2(e) shows the DC plots of LYCB, LYB, and LYC, revealing comparable electronic conductivities for all three, below 2×10^{-9} S/cm.

3.3 Electrochemical performance of LYCB

LYCB exhibits a remarkable enhancement in ion conductivity compared to LYC and LYB synthesized using the wet chemistry approach. To further investigate the electrochemical performance of LYCB, CV cells and ASSLBs were assembled for comparative testing, as illustrated in Fig. 3(a). Detailed specifications of all cells can be found in the experimental section, and the XRD pattern from the LPSC is shown in Fig. S5 in SI. It is important to note that the optimal mass fraction of LYX in the composite cathode of the ASSLBs is approximately 40%, as reported in the literature [35]. However, as mentioned earlier, there are significant density differences among the three electrolytes. Therefore, even with the same mass fraction, the actual contact between NCM811 and the electrolyte in the three batteries is different. Hence, to facilitate experimental and literature comparisons, a composite with mass fraction of 37% is adopted, even though it may not represent the optimal composition for each electrolyte. Nevertheless, maintaining consistent actual contact conditions also necessitates considering factors such as particle size and morphology.

Figure 3(b) presents the CV curves of LYCB, LYB and LYC, with voltage vs Li^+/Li–In. It can be observed that the first oxidation peak of LYCB occurs at a lower voltage (2.5 V) with a minimal polarization current, followed by the main oxidation peak at 3.2 V. Surprisingly, in the first cycle of oxidation and reduction, the oxidation peak of LYC appears at around 3 V, which is not only lower than 3.2 V of LYCB and LYB but also below the

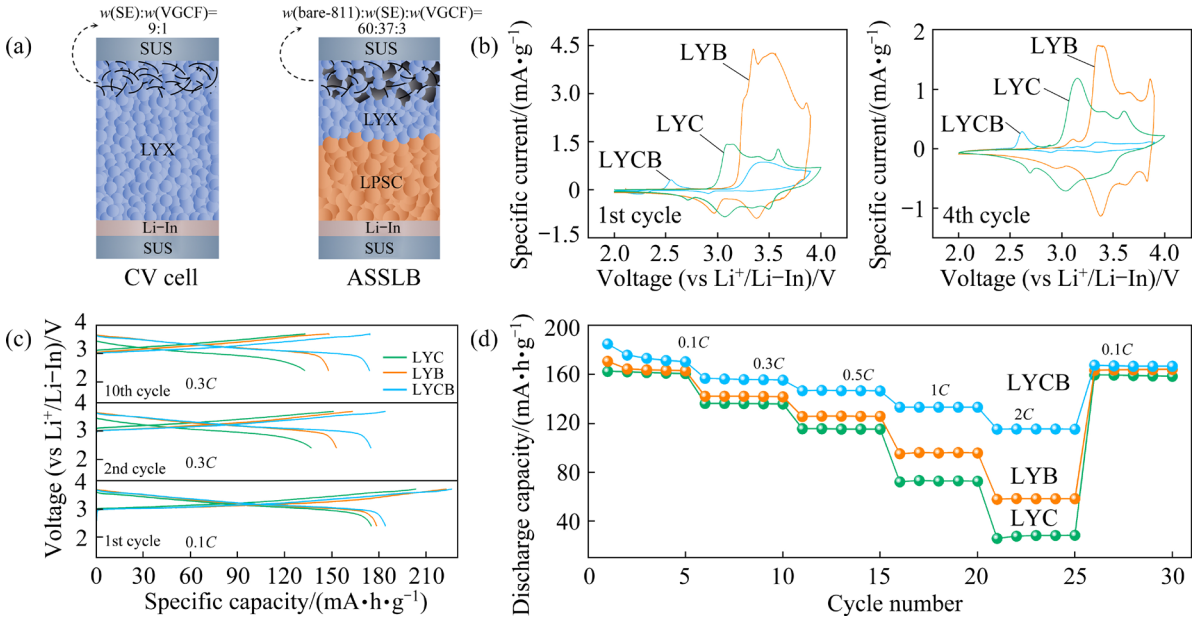

Fig. 3 Schematic illustrations of CV cell and ASSLBs structure (a); First and fourth cycle CV curves of LYCB, LYB, and LYC (b); Charge−discharge voltage profiles of LYCB, LYB, and LYC ASSLBs (c); Rate capabilities of LYCB, LYB, and LYC ASSLBs (d) (In ASSLBs, the loading of NCM811 is 7.64 mg/cm^2)

literature-reported 4 V (≈3.4 V vs Li$^+$/Li–In) [16]. This indicates that the degree of crystallinity not only influences the ionic conductivity of LYC but also impacts its electrochemical window. In general, the electrochemical window obtained from CV testing differs from theoretical calculations, primarily due to the impact of interfacial stability [17]. As shown in Fig. S2 in SI, the crystallinity of LYC particles is significantly higher than that of BM-LYC. High crystallinity can lead to reduced processability of the grains, resulting in poorer inter-particle bonding and weaker adhesion to the Li–In anode. This can easily cause localized over-polarization, leading to a decrease in the electrochemical window.

Furthermore, at high voltage, the specific current of LYB is twice that of LYC and LYCB. In the fourth cycle of oxidation and reduction, compared to the first cycle, the position and characteristic current of the first oxidation peak of LYCB at 2.5 V remain nearly unchanged, while the specific current of the second oxidation peak at 3.2 V significantly decreases, even lower than that at 2.5 V. Based on the characteristics of the CV curve, the oxidation process of LYCB at 3.2 V should be similar to that of LYC and LYB. However, it is evident that the specific current of LYCB decreases more significantly than that of LYC and LYB. By combining the phenomenon of the oxidation peak of LYCB at 2.5 V, it can be inferred that the oxidation behavior of LYCB at 2.5 V may weaken the subsequent oxidation effect. The oxidation peak of LYCB at 2.5 V appears to be irreversible, likely due to continuous decomposition during cycling. This leads to the accumulation of oxidation decomposition products, which form a passivation protective layer that prevents oxidation at 3.2 V. Therefore, LYCB exhibits excellent inherent oxidation stability, with an oxidation window close to 3.8 V (relative to Li$^+$/Li), and the oxidation products can also play a passivation role in subsequent oxidation. Additional information on the performance of LYCB at the limit voltage is provided in Fig. S6 in SI, where a voltage range from 0 to 5 V (vs Li$^+$/Li−In) is tested. It can be observed that the oxidation specific current of LYCB does not experience a substantial increase under high voltages of 4−5V (vs Li$^+$/Li−In). This observation suggests the potential of LYCB to serve as an electrolyte suitable for high-voltage cathode materials.

Figure 3(c) depicts the specific capacity−voltage curves of LYCB, LYB and LYC in the ASSLBs. During the testing, LYCB ASSLB exhibits an initial charge-specific capacity of 226 mA·h/g and a discharge-specific capacity of

184 mA·h/g, with an initial coulombic efficiency of 81.4%. These values are slightly higher than those of LYC and LYB ASSLBs. However, as the rate increases to 0.3*C*, the discharge specific capacity of LYCB ASSLB drops to 175 mA·h/g, while LYC ASSLB falls to 136.8 mA·h/g and LYB ASSLB to 152.8 mA·h/g. Overall, the differences in the initial efficiency and discharge-specific capacity among LYX ASSLBs are consistent with the differences in oxidation capabilities of LYX demonstrated in CV tests. Exactly, higher oxidation stability of the electrolyte leads to fewer side reactions with the active materials and less polarization consequently.

To further investigate the rate performance of LYCB, charge−discharge tests were conducted at rates ranging from 0.1*C* to 2*C*, as shown in Fig. 3(d). Interestingly, even at 2*C* rate, LYCB ASSLB still achieves a discharge capacity of 115 mA·h/g, significantly higher than 58 mA·h/g of LYB ASSLB and 38 mA·h/g of LYC ASSLB. However, below 0.5*C* rate, the difference in discharge-specific capacity among the three electrolytes is not pronounced. It is evident that the discharge specific capacity of the three electrolytes is positively correlated with their conductivity. However, the exceptional discharge specific capacity of LYCB at 2*C* cannot be explained solely by its high ionic conductivity. The by-products generated between the electrolyte and NCM811 during cycling, as well as the resulting interfacial changes, are equally important. Figure 4(a) presents long-term cycling performance of LYX ASSLBs. After 200 cycles at 0.3*C*, LYCB ASSLB has the highest discharge-specific capacity of 162 mA·h/g and the highest capacity retention rate of 93%. For the variations in resistance observed through EIS measurements, as shown in Fig. 4(b), LYCB ASSLB also has the lowest resistance after 200 cycles. The increase in resistance after cycling of ASSLB is mainly attributed to the generation of CEI and the slow diffusion rate of the internal phases in active materials. Therefore, broadening the electrolyte window and enhancing its chemical and electrochemical stability with active materials are crucial [36−38].

Moreover, the cross-sectional morphologies of the composite cathodes of LYCB and LYC ASSLBs before cycling and discharge to 2.4 V (vs Li^+/Li–In) after 200 cycles are depicted in Fig. 4(c). Before cycling, compared to LYC ASSLB, the LYCB ASSLB exhibits effective bonding between the electrolyte and NCM811. As shown in Fig. 2(b), the poor processability of LYC results in insufficient contact with NCM811, which negatively impacts the overall battery performance. Surprisingly, after 200 cycles, despite the cracking of NCM811, the

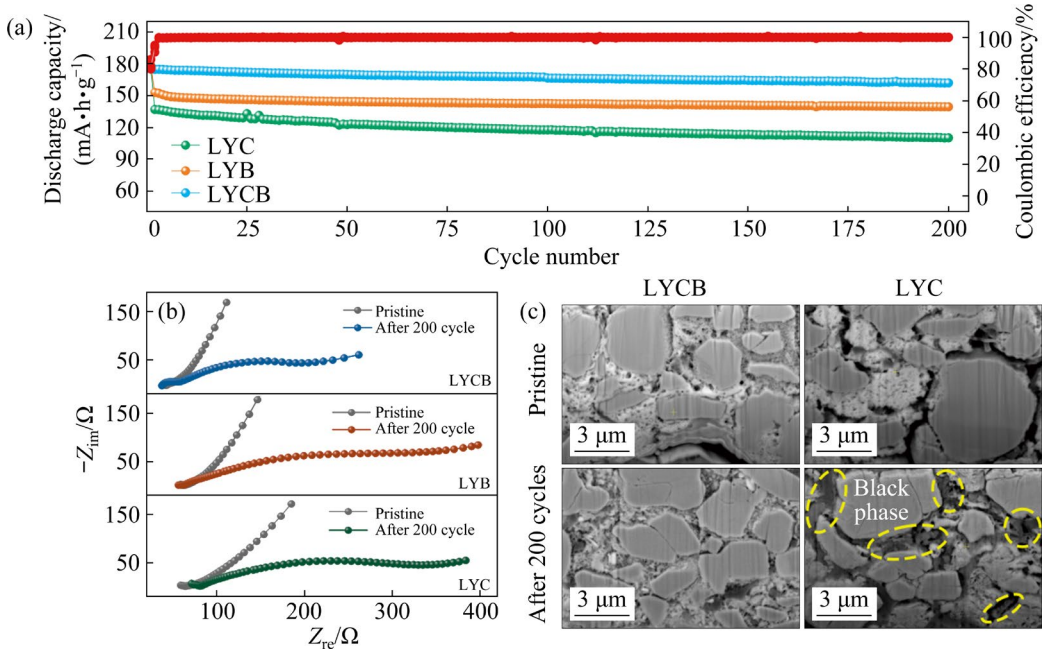

Fig. 4 Long-term cycling performances of LYCB, LYB, and LYC ASSLBs at 0.3*C* (a); Nyquist plots from 1 MHz to 0.01 Hz for LYCB, LYB, and LYC ASSLIBs after 200 cycles (b); Cross-sectional SEM-BSE images of composite cathodes for LYCB and LYC ASSLBs before and after cycling (c) (In ASSLBs, the loading of NCM811 is 7.64 mg/cm^2)

interface between LYCB and NCM811 is closer, and even the micropores in the LYCB tend to disappear. In addition, the interface between LYC and NCM811 is improved by a “black phase” after 200 cycles, which is suspected to be a by-product. Therefore, it is speculated that the by-products generated during the cycling process of LYCB and LYC play a role in improving interface contact. In summary, the by-products generated from the composite cathode of LYX ASSLBs influence the transport status of lithium ions and electrons during cycling, consequently affecting their battery performance.

3.4 Analysis of degradation products

According to previous studies [36,39], the main reaction product of LYC with oxide cathode materials under high pressure is YClO. XPS tests were conducted on the composite cathodes of LYX ASSLBs before cycling and discharge to 2.4 V (vs Li^+/Li−In) after 200 cycles, and the results are presented in Fig. 5. The Y 3d XPS spectra in Fig. 5(a) reveal the appearance of a new set of peaks (156.3 and 158.2 eV) after cycling in LYCB ASSLB. By comparing with the literature, it is observed that the binding energy position of the new peak is similar to that of Y_2O_3 [30,40]. In contrast, Figs. 5(b, c) demonstrate that the new component peaks observed in LYC and LYB ASSLB (157.3 and 159.3 eV) do not belong to Y_2O_3. Additionally, Figs. 5(d, e) show that after 200 cycles, a new spectral peak of O 1s appears in the LYCB ASSLB, while this does not occur in LYC and LYB ASSLBs. Furthermore, the adsorption oxygen (C—O) peaks in LYB and LYC almost completely disappear after 200 cycles. Information regarding Cl 2p and Br 3d can be found in Fig. S7 in SI, where no significant changes in XPS spectra are observed across the three ASSLBs. Thus, the oxidative decomposition behavior of LYCB is noticeably different from that of LYB and LYC. It is speculated that the oxidative reaction between LYCB and NCM811 is more inclined to generate Y_2O_3, whereas LYC and LYB tend to produce YClO or YBrO when reacting with NCM811 [36,39].

To further understand the phase evolution of LYCB, TEM analysis was conducted on NCM811 particles before and after 200 cycles, as shown in Figs. 6(a−c). Notably, to minimize disruption of the by-products, prolonged ultrasonic treatment was used during sample preparation instead of dissolving the solid electrolyte. Before cycling, no

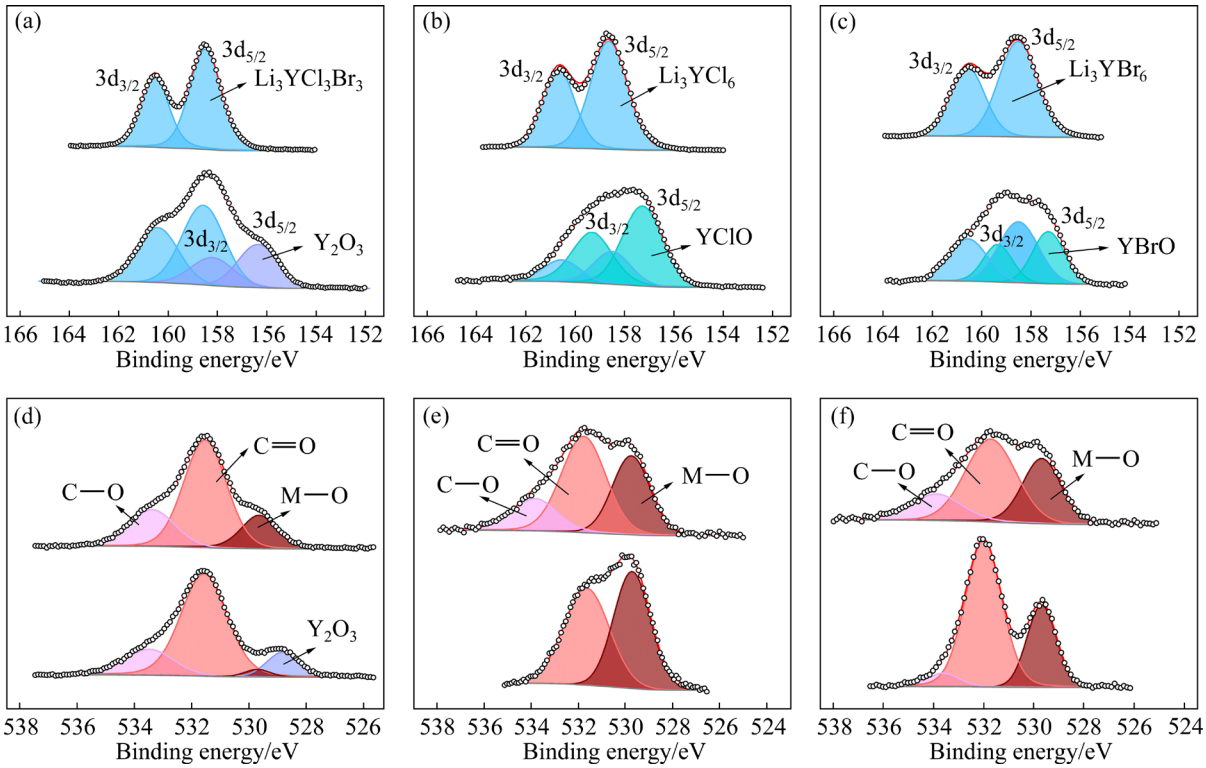

Fig. 5 Y 3d XPS spectra of composite cathode for LYCB (a), LYB (b), and LYC (c) ASSLBs after 200 cycles; O 1s XPS spectra of composite cathode for LYCB (d), LYB (e), and LYC (f) ASSLBs after 200 cycles

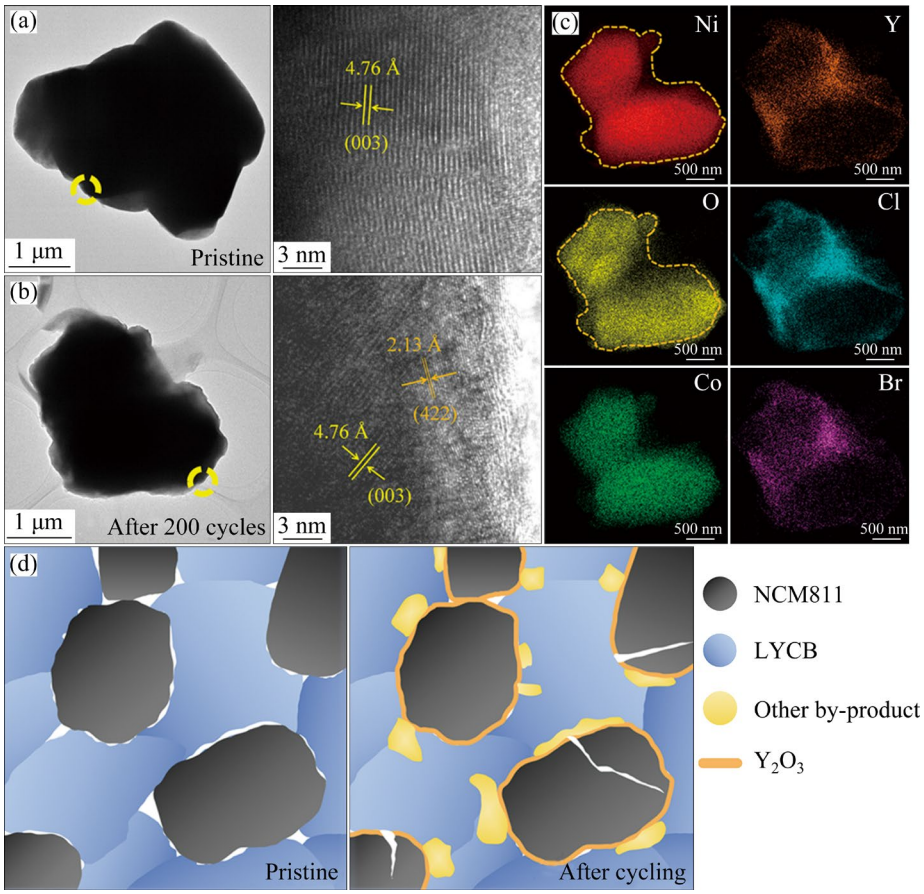

Fig. 6 TEM images of NCM811 particles and FFT images for corresponding surface regions before cycling (a) and after 200 cycles (b) in composite cathode of LYCB ASSLBs; Surface mapping of grains (c); Schematic illustrating interfacial evolution in composite cathode of LYCB ASSLBs (d)

phase other than NCM811 is observed on the surface of the NCM811 particles. However, after cycling, distinct lattice fringes are observed on the surface of the NCM811 grains, with a measured lattice spacing of approximately 2.13 Å. The Comparison with the XRD phase database reveals a close similarity between the lattice spacing and the (012) plane of Y_2O_3 (PDF# 04-014-8969) with a lattice spacing of 2.16 Å. Additionally, as shown in Fig. 6(c), surface mapping of the grains indicates the outward diffusion of the O atom relative to the Ni atom, suggesting a relatively thin oxide layer. Moreover, there is no apparent oxidation within the electrolyte interior. By combining these results with the previous XPS analysis (Fig. 5), it can be concluded that an oxidative reaction occurs between LYCB and the surface of NCM811 during the charge−discharge cycling process, leading to the in-situ formation of Y_2O_3 on NCM811 particles.

Based on these findings, the interface evolution of the composite cathode in LYCB ASSLBs during long cycling can be summarized, as illustrated in Fig. 6(c). Before cycling, the LYCB exhibits relatively close contact with NCM811, although few cracks and micropores are present at the interface. After prolonged cycling, with the decomposition of LYCB and the structural degradation of NCM811, stable Y_2O_3 by-products are gradually generated in situ on the surface of NCM811. Y_2O_3 serves not only as an inert protective layer preventing reactions between LYCB and the internal lattice oxygen of NCM811 but also enhances the physical bonding at the interface. Furthermore, other decomposition by-products of LYCB (potentially LiCl or LiBr) immobilize the gaps and spaces between the electrolyte and electrolyte, as well as between the electrolyte and NCM811 [39]. Notably, Y_2O_3 is non-conductive for both lithium ions and electrons, which exhibits excellent thermodynamic and electrochemical stability. Therefore, Y_2O_3 functions as an inert protective layer between LYCB and

NCM811. However, Y_2O_3 acts as an impediment in the lithium-ion and electron transfer system, and an excessively thick Y_2O_3 layer may adversely affect the stability of ultra-long cycling. Nevertheless, LYCB ASSLBs still possess significant advantages compared to LYC and LYB ASSLBs.

4 Conclusions

(1) LYCB was synthesized via an ammonia-assisted wet chemistry method. Compared to LYC and LYB, LYCB synthesized through this novel route exhibits higher ionic conductivity, reaching 2.08 mS/cm. Furthermore, LYCB possesses a high electrochemical window of 3.8 V, thereby establishing its stability and suitability for contemporary mainstream cathodes.

(2) In comparison to LYC and LYB ASSLBs, LYCB ASSLBs demonstrate superior performance, in which the initial coulombic efficiency achieved 81.4% under 0.3*C* cycling, and the capacity retention after 200 cycles reaches 93%. What's more, even under 2*C* cycling, the specific capacity remains close to 115 mA·h/g.

(3) It is found that the composite cathode of LYCB ASSLBs forms an in-situ Y_2O_3 inert protective layer on the surface of NCM811 under high voltage, effectively preventing further reactions between LYCB and NCM811.

(4) The above results validate the feasibility of composition adjustment in the wet chemistry synthesis route for halide solid electrolytes, offering a method for synthesis of halide solid electrolyte with two halogens.

CRediT authorship contribution statement

Han-zhou LIU: Conceptualization, Validation, Formal analysis, Investigation, Resources, Writing − Original draft, Review & editing; **Yan-chen LIU:** Validation, Investigation, Formal analysis; **Sheng-hao JING:** Validation, Investigation, Formal analysis; **Ya-qi HU:** Validation, Investigation, Formal analysis; **Zong-liang ZHANG:** Methodology, Supervision, Writing − Review & editing; **Si-liang LIU:** Methodology, Supervision, Writing − Review & editing; **Yang LIU:** Funding acquisition, Resources; **Zhi ZHUANG:** Funding acquisition, Resources; **Fan-qun LI:** Funding acquisition, Resources; **Fang-yang LIU:** Writing − Review & editing, Visualization, Supervision, Funding acquisition, Resources.

Declaration of competing interest

The authors declare that they have no known competing financial interests or personal relationships that could have appeared to influence the work reported in this paper.

Acknowledgments

This work was financially supported by Hunan Provincial Science and Technology Department, China (No. 2021JJ10058), and Key Research and Development Program of Hunan Province, China (No. 2023GK2016).

Supporting Information

The Supporting Information in this paper can be found at: http://tnmsc.csu.edu.cn/download/16-p2341-2024-0654-Supporting-Information.pdf.

References

[1] LI M, LU Jun, CHEN Zhong-wei. AMINE K. 30 years of lithium-ion batteries [J]. Advanced Materials, 2018, 30: e1800561.

[2] BANERJEE A, WANG Xue-feng, FANG Cheng-cheng, WU E A, MENG Y S. Interfaces and interphases in all-solid-state batteries with inorganic solid electrolytes [J]. Chemical Reviews, 2020, 120: 6878−6933.

[3] LI Fang-cheng, ZHANG Gang, ZHANG Zong-liang, YANG Jian, LIU Fang-yang, JIA Ming, JIANG Liang-xing. Regeneration of Al-doped $LiNi_{0.5}Co_{0.2}Mn_{0.3}O_2$ cathode material by simulated hydrometallurgy leachate of spent lithium-ion batteries [J]. Transactions of Nonferrous Metals Society of China, 2022, 32: 593−603.

[4] GAO Zhong-hui, SUN Hai-bin, FU Lin, YE Fang-liang, ZHANG Yi, LUO Wei, HUANG Yun-hui. Promises, challenges, and recent progress of inorganic solid-state electrolytes for all-solid-state lithium batteries [J]. Advanced Materials, 2018, 30: e1705702.

[5] FENG Xu-yong, FANG Hong, WU Nan, LIU Peng-cheng, JENA P, NANDA J, MITLIN D. Review of modification strategies in emerging inorganic solid-state electrolytes for lithium, sodium, and potassium batteries [J]. Joule, 2022, 6: 543−587.

[6] ZHANG Qian, LIU Kun, WEN Ya-jing, KONG Ya-qi, WEN Yu-hao, ZHANG Qi, LIU Nai-liang, LI Jun-peng, MA Chun-jie, DU Ya-ping. Advances in solid lithium ion electrolyte based on the composites of polymer and LLTO/LLZO of rare earth oxides [J]. Engineering Reports, 2021, 4: e12448.

[7] GEIGER C A, ALEKSEEV E, LAZIC B, FISCH M, ARMBRUSTER T, LANGNER R, FECHTELKORD M, KIM N, PETTKE T, WEPPNER W. Crystal chemistry and stability of "$Li_7La_3Zr_2O_{12}$" garnet: A fast lithium-ion conductor [J]. Inorganic Chemistry, 2011, 50: 1089−1097.

[8] GUO Zhi-hao, LI Xin-hai, WANG Zhi-xing, GUO Hua-jun, PENG Wen-jie, HU Qi-yang, YAN Guo-chun, WANG Jie-xi. Empirical decay relationship between ionic conductivity and

porosity of garnet type inorganic solid-state electrolytes [J]. Transactions of Nonferrous Metals Society of China, 2022, 32: 3362−3373.

[9] NIE Kai-hui, WANG Xue-long, QIU Ji-liang, WANG Yi, YANG Qi, XU Jing-jing, YU Xi-qian, LI Hong, HUANG Xue-jie, CHEN Li-quan. Increasing poly(ethylene oxide) stability to 4.5 V by surface coating of the cathode [J]. ACS Energy Letters, 2020, 5: 826−832.

[10] LIU Shuai-lei, LIU Wen-yi, BA De-liang., ZHAO Yong-zhi, YE Yi-hua, LI Yuan-yuan, LIU Jin-ping. Filler-integrated composite polymer electrolyte for solid-state lithium batteries [J]. Advanced Materials, 2023, 35: e2110423.

[11] KAMAYA N, HOMMA K, YAMAKAWA Y, HIRAYAMA M, KANNO R, YONEMURA M, KAMIYAMA T, KATO Y, HAMA S, KAWAMOTO K, MITSUI A. A lithium superionic conductor [J]. Nature Materials, 2011, 10: 682.

[12] ZENG De-wu., YAO Jing-ming, ZHANG Long, XU Ruo-nan, WANG Shao-jie, YAN Xin-lin, YU Chuang, WANG Lin. Promoting favorable interfacial properties in lithium-based batteries using chlorine-rich sulfide inorganic solid-state electrolytes [J]. Nature Communications, 2022, 13: 1909.

[13] KATO Y, HORI S, SAITO T, SUZUKI K, HIRAYAMA M, MITSUI A, YONEMURA M, IBA H, KANNO R. High-power all-solid-state batteries using sulfide superionic conductors [J]. Nature Energy, 2016, 1: 16030.

[14] OHNO S, ROSENBACH C, DEWALD G F, JANEK J, ZEIER W G. Linking solid electrolyte degradation to charge carrier transport in the thiophosphate-based composite cathode toward solid-state lithium-sulfur batteries [J]. Advanced Functional Materials, 2021, 31: 2010620.

[15] JING Sheng-hao, SHEN Hua-qing, HUANG Yu-ting, KUANG Wu-qi, ZHANG Zong-liang, LIU Si-liang, YIN Shuo, LAI Yan-qing, LIU Fang-yang. Toward the practical and scalable fabrication of sulfide-based all-solid-state batteries: exploration of slurry process and performance enhancement via the addition of $LiClO_4$ [J]. Advanced Functional Materials, 2023, 33: 2214274.

[16] ASANO T, SAKAI A, OUCHI S, SAKAIDA M, MIYAZAKI A, HASEGAWA S. Solid halide electrolytes with high lithium-ion conductivity for application in 4 V class bulk-type all-solid-state batteries [J]. Advanced Materials, 2018, 30: 1803075.

[17] NIKODIMOS Y, SU W N, HWANG B J. Halide solid-state electrolytes: Stability and application for high voltage all-solid-state Li batteries [J]. Advanced Energy Materials, 2022, 13: 2202854.

[18] KWAK H, KIM J S, HAN D, KIM J S, PARK J, KWON G, BAK S M, HEO U, PARK C, LEE H W, NAM K W, SEO D H, JUNG Y S. Boosting the interfacial superionic conduction of halide solid electrolytes for all-solid-state batteries [J]. Nature Communications, 2023, 14: 2459.

[19] LI Xiao-na, LIANG Jian-wen, CHEN Ning, LUO Jing, ADAIR K R, WANG Chang-hong, BANIS M N, SHAM T K, ZHANG Li, ZHAO Shang-qian, LU Shi-gang, HUANG Huan, LI Ru-ying, SUN Xue-liang. Water-mediated synthesis of a superionic halide solid electrolyte [J]. Angewandte Chemie International Edition, 2019, 58: 16427−16432.

[20] LI Xiao-na, LIANG Jian-wen, LUO Jing, NOROUZI B M, WANG Chang-hong, LI Wei-han, DENG Si-xu, YU Chuang, ZHAO Fei-peng, HU Yong-feng, SHAM T K, ZHANG Li, ZHAO Shang-qian, LU Shi-gang, HUANG Huan, LI Ru-ying, ADAIR K R, SUN Xue-liang. Air-stable Li_3InCl_6 electrolyte with high voltage compatibility for all-solid-state batteries [J]. Energy & Environmental Science, 2019, 12: 2665.

[21] LIANG Jian-wen, LI Xiao-na, WANG Shuo, ADAIR K R, LI Wei-han, ZHAO Yang, WANG Chang-hong, HU Yong-feng, ZHANG Li, ZHAO Shang-qian, LU Shi-gang, HUANG Huan, LI Ru-ying, MO Yi-fei, SUN Xue-liang. Site-occupation-tuned superionic Li_xScCl_{3+x}halide solid electrolytes for all-solid-state batteries [J]. Journal of the American Chemical Society, 2020, 142: 7012−7022.

[22] LIU Zhan-tao, MA Shu-an, LIU Jue, XIONG Shan, MA Yi-fan, CHEN Hai-long. High ionic conductivity achieved in $Li_3Y(Br_3Cl_3)$ mixed halide solid electrolyte via promoted diffusion pathways and enhanced grain boundary [J]. ACS Energy Letters, 2020, 6: 298−304.

[23] KIM S Y, KAUP K, PARK K H, ASSOUD A, ZHOU L, LIU J, WU X, NAZAR L F. Lithium ytterbium-based halide solid electrolytes for high voltage all-solid-state batteries [J]. ACS Materials Letters, 2021, 3: 930.

[24] WANG Kai, REN Qing-yong, GU Zhen-qi, DUAN Chao-min, WANG Jin-zhu, ZHU Feng, FU Yuan-yuan, HAO Ji-peng, ZHU Jin-feng, HE Lun-hua, WANG Chin Wei, LU Ying-ying, MA Jie, MA Cheng. A cost-effective and humidity-tolerant chloride solid electrolyte for lithium batteries [J]. Nature Communications, 2021, 12: 4410.

[25] KWAK H, HAN D, LYOO J, PARK J, JUNG S H, HAN Y, KWON G, KIM H, HONG S T, NAM K W, JUNG Y S. New cost-effective halide solid electrolytes for all-solid-state batteries: Mechanochemically prepared Fe^{3+}-substituted Li_2ZrCl_6 [J]. Advanced Energy Materials, 2021, 11: 2003190.

[26] LUO Xu-ming, WU Xian-zhang, XIANG Jia-yuan, CAI Dan, LI Min, WANG Xiu-li, XIA Xin-hui, GU Chang-dong, TU Jiang-ping. Heterovalent cation substitution to enhance the ionic conductivity of halide electrolytes [J]. ACS Applied Materials & Interfaces, 2021, 13: 47610−47618.

[27] SHAO Qi-nong, YAN Chen-hui, GAO Ming-xi, DU Wu-bin, CHEN Jian, YANG Ya-xiong, GAN Jian-tuo, WU Zhi-jun, SUN Wen-ping, JIANG Yin-zhu, LIU Yong-feng, GAO Ming-xia, PAN H. New insights into the effects of Zr substitution and carbon additive on $Li_{3-x}Er_{1-x}Zr_xCl_6$ halide solid electrolytes [J]. ACS Applied Materials & Interfaces, 2022, 14: 8095−8105.

[28] ZHOU Lai-dong, ZUO Tong-Tong, KWOK C Y, KIM S Y, ASSOUD A, ZHANG Qiang, JANEK J, NAZAR L F. High areal capacity, long cycle life 4 V ceramic all-solid-state Li-ion batteries enabled by chloride solid electrolytes [J]. Nature Energy, 2022, 7: 83−93.

[29] KWAK H, WANG Shuo, PARK J, LIU Yun-sheng, KIM K T, CHOI Y, MO Yi-fei, JUNG Y S. Emerging halide superionic conductors for all-solid-state batteries: Design, synthesis, and practical applications [J]. ACS Energy Letters, 2022, 7: 1776−1805.

[30] WANG Chang-hong, LIANG Jian-wen, LUO Jing, LIU Jue, LI Xiao-na, ZHAO Fei-peng, LI Ru-ying, HUANG Huan, ZHAO Shang-qian, ZHANG Li, WANG Jian-tao, SUN

Xue-liang. A universal wet-chemistry synthesis of solid-state halide electrolytes for all-solid-state lithium-metal batteries [J]. Science Advances, 2021, 7: eabh1896.

[31] MEYER G, GARCIA E, CORBETT J D. The ammonium chloride route to anhydrous rare earth chlorides — The example of YCl_3 [J]. Inorganic Syntheses, 1989, 25: 146−150.

[32] FENG Xu-yong, CHIEN P H, WANG Yan, PATEL S, WANG Peng-bo, LIU Hao-yu, IMMEDIATO-SCUOTTO M, HU Yan-Yan. Enhanced ion conduction by enforcing structural disorder in Li-deficient argyrodites $Li_{6-x}PS_{5-x}Cl_{1+x}$ [J]. Energy Storage Materials, 2020, 30: 67−73.

[33] HE Xing-feng, ZHU Yi-zhou, MO Yi-fei. Origin of fast ion diffusion in super-ionic conductors [J]. Nature Communications, 2017, 8: 15893.

[34] STEFANO D D, MIGLIO A, ROBEYNS K, FILINCHUK Y, LECHARTIER M, SENYSHYN A, ISHIDA H, SPANNENBERGER S, PRUTSCH D, LUNGHAMMER S, RETTENWANDER D, WILKENING M, ROLING B, KATO Y, HAUTIER G. Superionic diffusion through frustrated energy landscape [J]. Chem, 2019, 5: 2450−2460.

[35] HAN Y, JUNG S H, KWAK H, JUN S, KWAK H H, LEE J H, HONG S T, JUNG Y S. Single- or poly-crystalline Ni-rich layered cathode, sulfide or halide solid electrolyte: Which will be the winners for all-solid-state batteries? [J]. Advanced Energy Materials, 2021, 11: 2100126.

[36] KOCHETKOV I, ZUO Tong-Tong, RUESS R, SINGH B, ZHOU Lai-dong, KAUP K, JANEK J, NAZAR L. Different interfacial reactivity of lithium metal chloride electrolytes with high voltage cathodes determines solid-state battery performance [J]. Energy & Environmental Science, 2022, 15: 3933−3944.

[37] ZUO Tong-Tong, RUESS R, PAN Rui-jun, WALTHER F, ROHNKE M, HORI S, KANNO R, SCHRODER D. JANEK J. A mechanistic investigation of the $Li_{10}GeP_2S_{12}$|$LiNi_{1-x-y}Co_xMn_yO_2$ interface stability in all-solid-state lithium batteries [J]. Nature Communications, 2021, 12: 6669.

[38] LU Yang, ZHAO Chen-Zi, HUANG Jia-Qi, ZHANG Qiang. The timescale identification decoupling complicated kinetic processes in lithium batteries [J]. Joule, 2022, 6: 1172−1198.

[39] CHUN G H, SHIM J H, YU S. Computational investigation of the interfacial stability of lithium chloride solid electrolytes in all-solid-state lithium batteries [J]. ACS Applied Materials & Interfaces, 2022, 14: 1241−1248.

[40] COLE K M, KIRK D W, THORPE S J. Surface Y_2O_3 layer formed on air exposed Y powder characterized by XPS [J]. Surface Science Spectra, 2020, 27: 024010.

采用湿化学法制备用于全固态电池的高性能 $Li_3YCl_3Br_3$ 固态电解质

刘汉周[1]，刘彦辰[1]，景圣皓[1]，胡雅琪[1]，张宗良[2]，
刘丝靓[3]，刘 洋[4]，庄 志[4]，李凡群[5]，刘芳洋[1,6]

1. 中南大学 冶金与环境学院，长沙 410083；
2. 中南大学 增值冶金湖南省重点实验室，长沙 410083；
3. 中南大学 先进电池材料教育部工程研究中心，长沙 410083；
4. 湖南恩捷前沿新材料科技有限公司，长沙 410208；
5. 万向一二三股份公司，杭州 311200；
6. 中南大学 国家能源金属资源与新材料重点实验室，长沙 410083

摘 要：采用湿化学法代替传统的机械球磨法合成了含有双卤素的固态电解质 $Li_3YCl_3Br_3$。研究表明，$Li_3YCl_3Br_3$ 具有 2.08 mS/cm 的离子电导率和 3.8 V 的电化学窗口。此外，以 $LiNi_{0.83}Co_{0.11}Mn_{0.06}O_2$(NCM811)为正极材料的 $Li_3YCl_3Br_3$ 基全固态锂离子电池在 0.3*C* 倍率下循环 200 次后容量保持率达 93%，在 2*C* 倍率下循环时仍保持 115 mA·h/g 的比容量。这归因于 $Li_3YCl_3Br_3$ 固有的高氧化稳定性，及高电压下其在 NCM811 表面原位形成的 Y_2O_3 惰性保护层。验证了使用简单低成本的湿化学法路线制备多组分卤化物的可行性，展示了卤化物固体电解质可规模化生产的应用潜力。

关键词：卤化物固体电解质；全固态电池；湿化学法；副产物；惰性层

(Edited by Bing YANG)